ELSEVIER

Contents lists available at ScienceDirect

# Chemical Engineering Journal

journal homepage: www.elsevier.com/locate/cej



# Enhanced photocatalytic and photothermal properties of ecofriendly metalorganic framework heterojunction for rapid sterilization



Yue Luo<sup>a</sup>, Xiangmei Liu<sup>a,\*</sup>, Lei Tan<sup>a</sup>, Zhaoyang Li<sup>b</sup>, Kelvin Wai Kwok Yeung<sup>c</sup>, Yufeng Zheng<sup>d</sup>, Zhenduo Cui<sup>b</sup>, Yanqin Liang<sup>b</sup>, Shengli Zhu<sup>b</sup>, Changyi Li<sup>e</sup>, Xianbao Wang<sup>a</sup>, Shuilin Wu<sup>b,\*</sup>

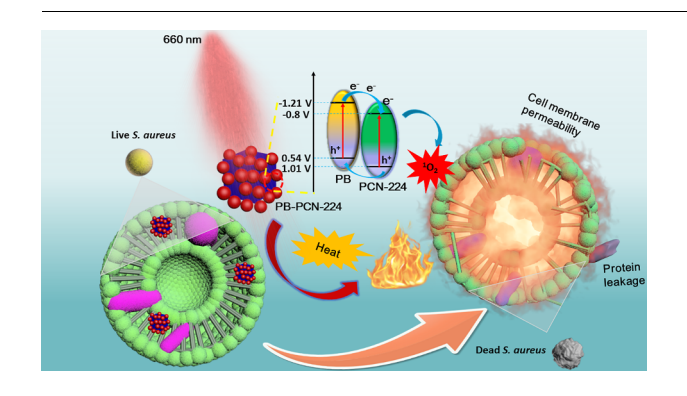
- <sup>a</sup> Ministry-of-Education Key Laboratory for the Green Preparation and Application of Functional Materials, Hubei Key Laboratory of Polymer Materials, School of Materials Science & Engineering, Hubei University, Wuhan 430062, China
- b School of Materials Science & Engineering, the Key Laboratory of Advanced Ceramics and Machining Technology by the Ministry of Education of China, Tianjin University, Tianjin 300072, China
- c Department of Orthopaedics & Traumatology, Li KaShing Faculty of Medicine, The University of Hong Kong, Pokfulam, Hong Kong 999077, China
- d State Key Laboratory for Turbulence and Complex System and Department of Materials Science and Engineering, College of Engineering, Peking University, Beijing 100871. China
- <sup>e</sup> Stomatological Hospital, Tianjin Medical University, No. 12, Qixiangtai Road, Heping District, Tianjin 300070, China

## HIGHLIGHTS

# The metal organic framework heterojunction of PB-PCN-224 was prepared.

- MOFs promotes charge transfer and inhibits recombination of electronhole pairs.
- PB-PCN-224 had good absorption in visible light.
- The compound had good photodynamic and photothermal effects.
- PB-PCN-224 had 99.84% and 99.3% antibacterial rate for S. aureus and its biofilm.

## GRAPHICAL ABSTRACT



## ARTICLEINFO

Keywords:
Wound healing
Photoresponsive
Metal-organic framework
Antibacterial
Heterojunction

## ABSTRACT

Injured tissues are susceptible to infections that suppress wound healing. Rapid and safe sterilization is therefore urgent for bacteria-infected wounds, especially under harsh conditions without antibiotic availability. In this work, we developed a photoresponsive metal–organic framework (MOF) heterojunction that responds to 660 nm light irradiation. It is composed of two kinds of MOFs (Prussian blue [PB] and PCN-224), which exhibited an enhanced photocatalytic performance due to the accelerated charge transfer of the heterojunction and the fast separation of photogenerated electron-hole pairs between PB and PCN-224. The combination of the enhanced photocatalytic performance and the intrinsic photothermal effect of PB endowed the MOFs heterojunction with highly effective sterilizing rates of 99.84% and 99.3% against *Staphylococcus aureus* and its biofilm after 660 nm light irradiation for 15 min, respectively. The iron and zirconium ions released from PB-PCN-224 composites were biocompatible and their cytotoxicity was negligible. More importantly, *in vivo* experiments showed that PB-PCN-224 can expedite wound healing.

E-mail addresses: liuxiangmei1978@163.com (X. Liu), shuilinwu@tju.edu.cn (S. Wu).

<sup>\*</sup> Corresponding authors.

#### 1. Introduction

An injury to the skin may interfere with the integrity of the epidermis, dermis, connective tissue, and microcirculation, thereby inevitably leading to a wound [1]. Wound healing is a dynamic and complex multicellular process involving extracellular matrix, cytokines and many other factors [2]. Healing can be further complicated by infections with bacteria such as *Staphylococcus aureus* (*S. aureus*), a common skin and wound pathogen [3,4]. Therefore, research that focused on rapid promotion of wound healing and elimination of bacterial infections is particularly important.

In recent years, many materials have been developed for wound sterilization, including metal ion fungicides [5,6], inorganic material fungicides [7,8], organic material fungicides, and antibiotics [9–12], but these materials have undesirable properties, such as biological toxicity and low biocompatibility. In addition, the overuse of antibiotics can lead to the emergence of drug-resistant bacteria [13]. Hence, novel, portable, and inexpensive measures without adverse effects are needed to combat microbial wound infections.

Some photoresponsive materials, such as IR-780 [14],  $\rm TiO_2$  [15],  $\rm Cu_2MoS_4$  [16],  $\rm MoS_2$  [17], and Prussian blue (PB) [18], have been developed to kill germs or anticancer via the generation of reactive oxygen species (ROS) or by hyperthermia. The corresponding strategies are termed photodynamic therapy (PDT) and photothermal therapy (PTT). ROS and hyperthermia can kill bacteria independently. However, excessive concentrations of ROS or temperatures above 60 °C may be harmful to normal cells and tissues [19,20]. For this reason, therapies that employ both strategies, by combining PDT with a low ROS generation and PTT at a temperature below 60 °C, are often employed to kill bacteria effectively while maintaining sufficient biosafety [21,22].

One material that would favor this type of combined strategy is the metal organic framework (MOF), an inorganic-organic hybrid material consisting of organic ligands and metal nodes (metal ions or clusters) linked by coordinate bonds [23]. MOFs have attracted much attention because of their large specific surface area, high porosity, and adjustable metal nodes or organic ligands. MOFs have been widely used in many fields, including gas adsorption [24], biomedicine [25], and catalysis [26]. MOFs, as a semiconductor material, have also been broadly studied as photocatalysts [27], as the bridging ligands in MOFs can act as antennas that adsorb light and convert the light energy to charges [28,29]. However, the key limitation to the effective use of MOF-based photocatalysts is the inability to enhance their light absorption and conversion efficacy under visible light at long

wavelengths. Other bottlenecks preventing high photocatalytic performance of these materials include a lack of methods for separating the photogenic electron hole pair and improving the charge separation [30].

Photosensitive organic molecules, such as porphyrins, can be incorporated into the MOF as bridging ligands to obtain a wider optical absorption range in the visible region. The ubiquity of natural or synthetic porphyrin ligands in these materials is attributed to the versatility of porphyrins in catalysis, light collection, and oxygen conversion [31]. The PCN is a well-known family of this type of MOF, and the Zr-based porphyrin MOF is now attracting extensive attention for its rich structural types, excellent chemical stability, and adjustable functionality [32]. However, these single-group spectroscopic catalysts are susceptible to rapid electron-hole recombination; therefore, they must be combined with other functional materials to form heterogeneously structured photocatalysts that can facilitate charge transfer from photoelectrons [33].

In this paper, we combined nanoparticles of the FDA-approved photothermal agent Prussian blue (PB) with a porphyrin metal organic framework (PCN-224). When irradiated with 660 nm red light, PCN-224 increased the shift efficiency of electrons generated from PB, thereby delaying the recombination of electron hole pairs and increasing the ROS yield of PB-PCN-224. At the same time, the introduction of PB endowed PB-PCN-224 with a good photothermal effect under 660 nm light irradiation. This synergy of PDT and PTT resulted in a 99.84% and 99.3% antibacterial rate against *S. aureus* and its biofilm, respectively, for PB-PCN-224. Scheme 1 shows this rapid bactericidal response of PB-PCN-224.

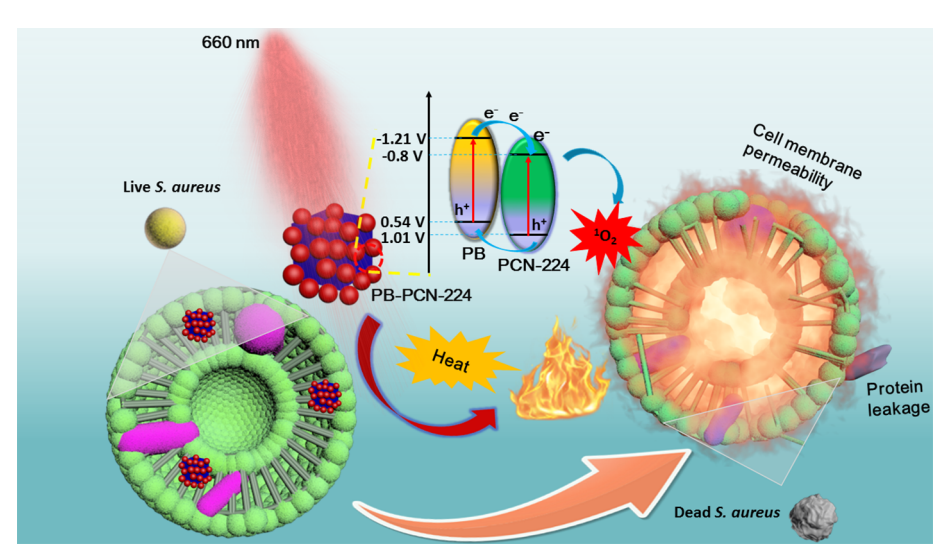
## 2. Experimental section

# 2.1. Preparation of PB

The PB nanoparticles were prepared by a simple method. Typically, 3 g PVP and 226.7 mg  $K_3[Fe(CN)_6]$  were dissolved in 40 mL HCl (0.01 M) and stirred in a 50 mL reactor for 30 min. The reactor was then placed into a furnace and heated for 20 h at 80 °C. The precipitates were centrifuged and washed five times with deionized water and with ethanol. The products were collected after drying for 12 h at 80 °C.

# 2.2. Synthesis of PB-PCN-224

A 30 mg sample of zirconium oxychloride octachloride (ZrOCl<sub>2</sub>·8H<sub>2</sub>O) was combined with 10 mg tetrakis(4-carboxyphenyl)



Scheme 1. Schema revealing the synergy of the ROS and photothermal effects in the germ-killing response of PB-PCN-224 under 660 nm light irradiation.

porphyrin (TCPP), 2.8 g benzoic acid (BA), 10 mg PB, and 10 mL of N,N-Dimethylformamide (DMF) and the mixed solution was then reacted at 90  $^{\circ}\text{C}$  in an oil bath at 300 rpm for 5 h. The compound was allowed to cool to room temperature and then washed three times with DMF and with ethanol. The precipitates were then placed into a 60  $^{\circ}\text{C}$  furnace to dry for 12 h.

## 2.3. Characterization

The morphologies and sizes of materials were inspected by transmission electron microscopy (TEM, Tecnai G20, FEI, USA) and field emission scanning electron microscopy (FE-SEM, ZEISS Sigma 500). The crystalline structure of materials was determined by X-ray diffractometry (XRD, D8A25, Bruker, Germany) with a detection range from 3 to 80° and a step size of 0.02°. Fourier transform infrared (FTIR) images were recorded on a spectrometer (NICOLET iS10). The nitrogen adsorption and desorption curves of the materials at 77 K were determined by Brunauer-Emmett-Teller (BET) analysis (BK112T). The UV spectra were recorded with an ultraviolet-visible (UV-vis) spectrophotometer (UV-3600, Shimadzu, Japan). X-ray photoelectron spectra (XPS) were obtained with an ESCALAB 250Xi instrument (Thermo Scientific, USA). Inductively-coupled plasma atomic emission spectrometry (ICPAES) was conducted with an Optimal 8000 instrument (Perkin Elmer, US). Room temperature photoluminescence (PL) measurements were performed on a fluorescence spectrometer (LS-55, PE, USA).

# 2.4. Photothermal effect test

The photothermal effect of the materials was monitored with a thermal imager (Testo 875i, Testo Instruments International Trading (Shanghai) Co., Ltd) by irradiating 200  $\mu$ g/mL of different samples (phosphate buffer saline (PBS), PB, PCN-224, and PB-PCN-224) with 660 nm LED light (0.3 W/cm²) for 15 min. The temperature change of the materials was monitored with a thermal imager every three minutes and an image was captured. A thermal imager was used to monitor the temperature change of the PB-PCN-224 for three cycles of 15 min heating and 15 min cooling.

# 2.5. Electrochemical test

Samples (4.0 mg) were dispersed in 1 mL ethanol and then 800  $\mu$ L naphthene was added and dispersed by ultrasonication. Subsequently, 50  $\mu$ L of the resulting solution was dropped onto a piece of titanium 6 mm in diameter. Titanium flakes coated with sample were heated at 60 °C for 30 min. A standard three-electrode apparatus, with a platinum sheet and an Ag/AgCl electrode as the auxiliary and compared electrode, was used to study the photocurrent of the materials. The titanium plates deposited with materials were used as the working electrode in a CHI 660E electrochemical station (Shanghai Chenhua, China) equipped with the illumination source (660 nm light). The three electrodes were inserted into a beaker filled with 0.5 M Na<sub>2</sub>SO<sub>4</sub> electrolyte. The photoreaction of the prepared photoelectrode (i.e., I-t) was measured for 180 s by testing the photocurrent densities under a short-cut light illumination (light on/off cycle: 30 s) at a declinational potential of 0.5 V vs. Ag/AgCl.

# 2.6. Photodynamic test with 1,3-diphenylisobenzofuran (DPBF) and electron spin resonance spectroscopy (ESR)

The reaction of DPBF with  $^1O_2$  reduces the fluorescence intensity centered at 420 nm. Samples (200  $\mu$ g/mL) were first dispersed in DPBF solution (dissolved in dimethyl sulfone) and followed by irradiation under 660 nm red light (120 s, LED light, 0.3 W/cm²) and analysis with an enzyme marker. The ESR spectra were recorded on a JES-FA200 spectrometer. TEMP (50 mM) was used as a spin trap for the detection

of singlet oxygen during irradiation of samples by light. Spin traps were ESR silent but formed stable radicals with an ESR signal after donating electrons. Determination of •OH by electron paramagnetic ESR using 5,5-dimethyl-1-pyrroline-N-oxide (DMPO) as the spin-trapping agent in water, because •OH could react with DMPO rapidly to obtain DMPOOH.

## 2.7. Antibacterial test

The antibacterial capacities of the materials were assessed using *S. aureus* (ATCC 29 213) and *S. aureus* biofilm through a spread plate method. Firstly, 160  $\mu L$  of bacterial solution (1  $\times$  10  $^7$  CFU mL $^{-1}$ ) was mixed with the sample solution containing either 40  $\mu L$  of PBS or 1 mg/mL of PB, PCN-224, or PB-PCN-224 and the mixtures were transferred to a 96-well plate in two groups. The first group was illuminated for 15 min with the 660 nm light, while the second group was incubated in the dark for 15 min. After the illumination, 10  $\mu L$  of bacterial solution was extracted from each well and diluted 100-fold with Luria-Bertain (LB) medium. A 20  $\mu L$  volume of the diluted bacterial samples was applied to agar plates and cultured at 37 °C for 24 h.

The antiseptic effectiveness against *S. aureus* biofilm was determined as follows. A 200  $\mu L$  volume of bacterial culture was co-cultured in 96-well plates for 48 h at 37 °C. The bacterial suspension was replaced with 200  $\mu L$  of sterile Luria–Bertani (LB) medium every 12 h. The plates with *S. aureus* biofilm were then washed with sterilized PBS (pH = 7.4) and covered with 200  $\mu L$  of the different materials (PB, PCN-224, and PB-PCN-224; 1 mg/mL). The antibacterial steps above were then repeated. The bacterial colonies on the plates were photographed, and the antibacterial rate was determined by counting the number of colonies using the following formula (where A is the number of colonies):

Antibacterial efficiency (%) = (A in control group – A in experimental group)/A in control group  $\times$  100%

# 2.8. Bacterial morphology

The bacterial morphologies were examined by SEM after the anti-bacterial experiment. The bacteria were fixed by removing the bacterial slurry and adding 100  $\mu L$  2.5% glutaraldehyde to the 96 well-plate and reacting for 2 h. The bacteria were then dehydrated sequentially in a graded ethanol series for 15 min. The bacterial morphologies were examined by SEM after drying.

# 2.9. Fluorescence staining of Live/Dead bacteria and detection of intracellular reactive oxygen species

Live/Dead Bacterial Viability Kit (Molecular Probes, L-13152) was employed to evaluate the antibacterial ability of materials. Both live (green) and dead (red) bacteria were observed by a fluorescence microscope (IX73, Olympus, USA). DCFH-DA was used to detect the *intracellular reactive oxygen species*.

# 2.10. Protein leakage

The bacterial membrane damage was detected using bichinchonic acid (BCA) protein detection. At the end of the antibacterial experiment, 150  $\mu L$  of bacterial liquid was mixed with 150  $\mu L$  PBS, and the mixture was centrifuged. A 20  $\mu L$  sample of the suspension was added to 200  $\mu L$  of BCA reagent, and protein leakage was measured with a microplate reader.

# 2.11. In vitro cell experiment

The mouse fibroblast cell line (NIH-3T3, Tongji Hospital, Wuhan) was used in these experiments. The cells were co-cultured with samples

for 1 day. Samples containing NIH-3T3 cells were washed with sterile PBS, and the cells were immobilized with 4% formaldehyde for 10 min, followed by washing with PBS. FITC (YiSen, Shanghai) was then added for 30 min to stain the cells, which were then washed with PBS. DAPI (YiSen, Shanghai) was then added for 30 s to dye the cells, followed by washing with PBS. Images were captured from an inverted fluorescence microscope.

The 3-[4,5-dimethylthiazol-2-yl]-2,5-diphenyl tetrazoliumbromide (MTT) assay was used to assess the cytotoxicity of PB-PCN-224 (200  $\mu g/$  mL), PB (200  $\mu g/$  mL), and PCN-224 (200  $\mu g/$  mL). NIH-3 T3 cells were cultured in 96-well plates in cell nutrient medium for 24 h. The medium was then removed and new medium containing the samples (200  $\mu L$ , with a sample to medium ratio of 1:9) was added and culture was continued for a further 24 h. The culture medium was then replaced with MTT solution (200  $\mu L$ , 0.5 M) at 37 °C. After 4 h, the MTT solution was removed and 200  $\mu L$  of DMSO solution was added to the well and placed for 15 min on a shaker with continuous rotation. A 100  $\mu L$  volume of the supernatant was removed and its absorbance (OD) was measured at 490 nm in a microplate reader.

## 2.12. In vivo animal wound healing test

Male Wistar rats (180-200 g body weight) were provided by Beijing Weitong Lihua Experimental Animal Technology Co., Ltd. The Institute of Radiation Medicine, Chinese Academy of Medical Sciences authorized the test. The rats were housed singly in cages for 3 days and then randomly divided into the following three groups with three rats per group: control group (PBS), 3 M group (routine wound treatment, Minnesota Mining and Manufacturing Medical Equipment (Shanghai), Ltd), and test group (PB-PCN-224). After anesthesia with 16% chloral hydrate, the backs of rats were slashed and 20 µL diluted bacterial solution (108 CFU/mL) was added to the wound, along with 20 μL of either PBS (control group and 3 M group) or 200 ug/mL of PB-PCN-224 (test group). After illuminated with 660 nm light (0.3 W/cm<sup>2</sup>), the wound in the control group was bandaged with opaque sterile medical tape. The 3 M group was treated with a standard 3 M wound dressing applied to the wound. The wounds of the experimental group were tightly wrapped with nontransparent sterile medical tape. The rats were then housed at standard temperature.

The wounds were photographed at 2, 4, and 8 days after treatment. The tissues were dyed with Giemsa and hematoxylin/eosin (H&E) stains to assess the quantity of bacteria around the wounds and the course of wound healing. The primary organs (heart, liver, spleen, lung, and kidney) were harvested on day 8 and stained with H&E to evaluate the *in vivo* biotoxicity of the materials.

## 3. Results and discussion

## 3.1. Characterization

The TEM images of the samples showed pristine PB particles with an average diameter of 260 nm (Fig. 1a) and a spherical structure of the PCN-224 samples with a uniform size distribution of about 70 nm (Fig. S1), which were well accordance with the corresponding SEM images (Fig. S2a, S2b). The TEM image of PB-PCN-224 composite showed that PCN-224 had grown around the PB nanoparticles, possibly due to the presence of PVP molecules on the surface of the PB nanoparticles (Fig. 1b and Fig. S2c). As shown in Fig. S3a, the 0.50 nm, 0.36 nm and 0.24 nm lattice fringe spacing represented the (200), (220) and (420) plane of PB.[34] After attaching PCN-224, the lattice of PB had not changed (Fig. S3b). Possibly, the C=O groups in the PVP molecules had coordinated with zirconium ions [35], thereby facilitating the growth of PCN-224 on the surface of the PB nanoparticles. Moreover, as shown in Fig. S4, the zeta potentials of PB, PCN-224 and PB-PCN-224 were -23.2, -11.1 and -11.2 mV respectively, and the zeta potential data of PCN-224 and PB-PCN-224 were basically the same, indicating that PCN-224 grew around PB.

A crystal structure diagram for PB-PCN-224 was showed in Fig. 1c. Energy-dispersive X-ray spectroscopy (EDS) data confirmed that PB-PCN-224 contained all the elements those in PB and PCN-224, indicating the co-existence of the two kinds of MOFs (Fig. S2d, S2e, S2f). The subsequent TEM mapping further demonstrated the successful synthesis of PB-PCN-224 (Fig. 1d). When PCN-224 was grown on the surface of PB, zirconium appeared and was mainly distributed around PB, with a location of this element showing the same distribution was the same as that of PCN-224. X-ray diffraction (XRD) charts were used to establish the crystallographic structures of the materials (Fig. 1e). The observed diffraction peaks were consistent with previous reports and indicated a very high crystallinity of the PB [35]. When compared with PB alone, the PB-PCN-224 composite demonstrated the diffraction peaks of PB as well as peaks at  $2\theta = 4.591^{\circ}$ ,  $6.494^{\circ}$  and  $7.956^{\circ}$  which respectively represent the (002), (022) and (222) crystal planes of PCN-224 (Fig. S5) [36].

The basic structures of the PB, PCN-224, and PB-PCN-224 composites were further examined by Fourier transform infrared spectroscopy (FT-IR) (Fig. 1f). In the spectra, the peak at 2090 cm<sup>-1</sup> represented the stretching vibration of the C≡N bond in the PB nanoparticles, and the peak at 499 cm<sup>-1</sup> represented the bending vibration of Fe-C≡N-Fe [35]. In pure PCN-224, the asymmetric vibration absorption of C≔O bond in H<sub>2</sub>TCPP appeared at 1701 cm<sup>-1</sup> [37]. The peaks around at 1600–1500 cm<sup>-1</sup> were attributed to the stretching oscillation of C≔C bond in the benzene ring [36]. The C−H oscillating vibration of the pyrrole ring formed a triplet state belt at 1020, 985, and 966 cm<sup>-1</sup> [37]. All the main characteristic peaks of PB and PCN-224 appeared in the FT-IR spectrum of the coupled PB-PCN-224 hybrid material.

The nitrogen adsorption and desorption experiment revealed the porosity of the material. As shown in Fig. 1g, the specific surface area of PB-PCN-224 was 47.131  $\mbox{m}^2/\mbox{g}$ , smaller than that of PCN-224 (61.393  $\mbox{m}^2/\mbox{g})$ , but the pore sizes of PB-PCN-224 and PCN-224 were both 1.614 nm, confirming that the addition of PB could reduce the specific surface area of PB-PCN-224 (Fig. S6). Since the size of the pore remained essentially unchanged, the presence of PB did not appear to affect the pore size distribution.

The elementary composition of PB-PCN-224 was determined by XPS analysis. The Fe 2p XPS spectra showed that the binding energies of  ${\rm Fe}^{2+}$  2p<sub>3/2</sub> and 2p<sub>1/2</sub> were situated at 708.7 and 721.6 eV (Fig. S7a), while the peak at 713.07 eV could be attributed to partially oxidized  ${\rm Fe}^{3+}$  [38]. The three primary peaks of the N 1s indicated the existence of three chemically different types of nitrogen atoms =N- (399.3 eV), C-N ([Fe(CN)<sub>6</sub>]<sup>4-</sup>) (397.4 eV), and -NH (396.8 eV) (Fig. S7b) [39,40]. The C 1 s spectrum revealed the presence of C-H/C-C (284.2 eV), C-O (284.6 eV), O=C-O (288.4 eV), and C-N (285.5 eV) (Fig. S7c) [41]. The O 1s spectrum was shown in Fig. S7d. The Zr 3d spectrum showed the binding energies of 182.4 and 184.7 eV, belonging to Zr  ${\rm 3d_{5/2}}$  and Zr  ${\rm 3d_{3/2}}$ , respectively (Fig. S7e) [42].

# 3.2. Photoelectrochemical characterization and band structure

The UV-visible diffuse reflectance spectra were recorded to evaluate the optical properties of the samples. Fig. 2a shows the absorption of PCN-224, which was mainly in the visible region, but its absorption was relatively weak. The addition of PB significantly increased the absorption of PB-PCN-224 in the visible region, particularly at 500–800 nm. Therefore, PB-PCN-224 had a greater light absorption capacity than PCN-224. The photoluminescence (PL) of the materials was primarily due to the recombination of the photoinduced electrons and holes. Generally, the possibility of this photogenic electron-hole pair recombination of this material decreased as the fluorescence intensity decreased, indicating a better photocatalytic effect of this material [43]. The PL spectrum in Fig. 2b showed lower fluorescence intensity for PB-PCN-224 than for the other samples. This might reflect the fast shift of electrons from PB to PCN-224 down the heterojunction, which would

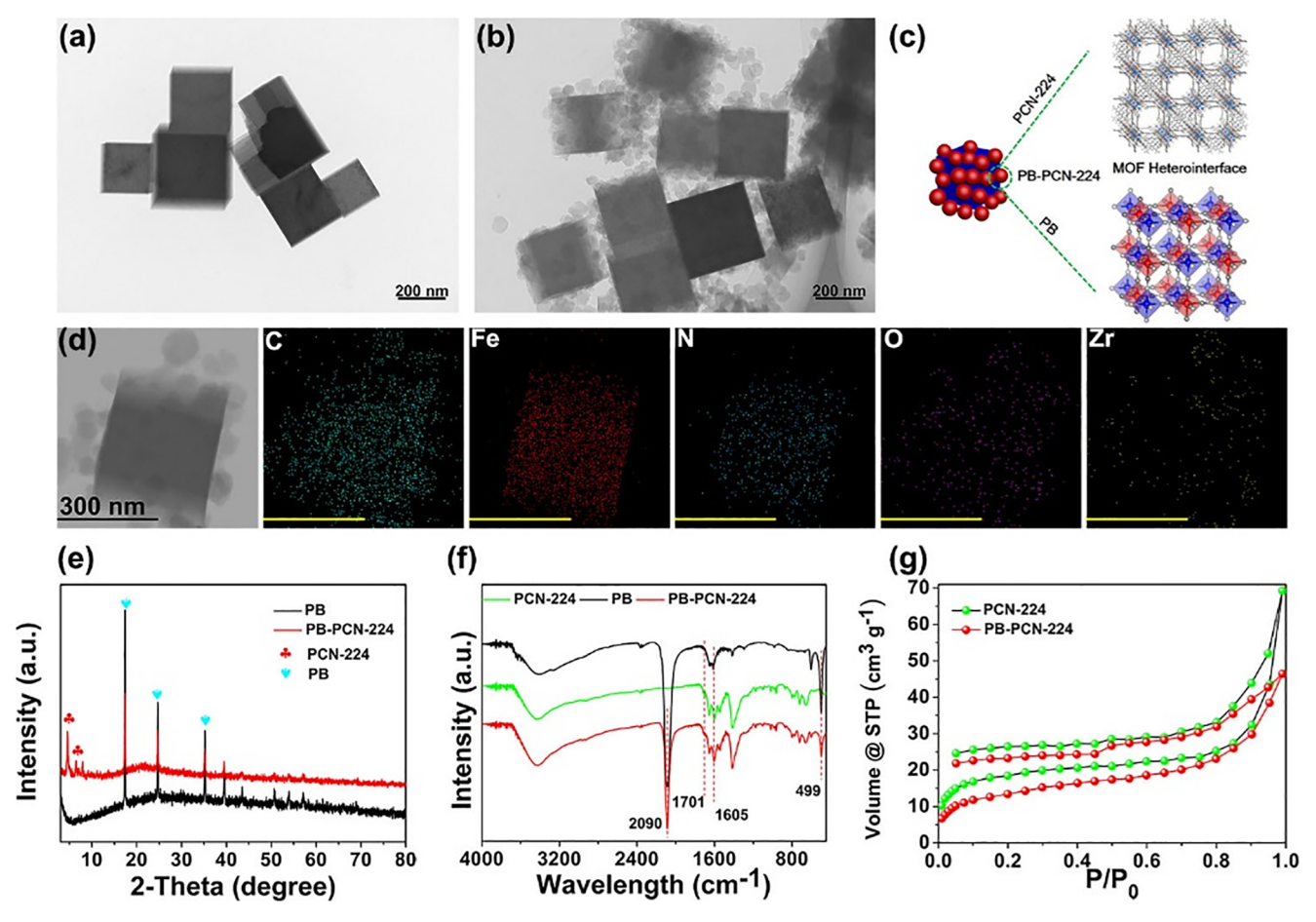


Fig. 1. Transmission electron microscopy (TEM) images of (a) Prussian blue nanoparticles (PB), and (b) PB-PCN-224; (c) The crystal structure diagram of PB-PCN-224; (d) High resolution TEM images of PB-PCN-224; (e) XRD of PB and PB-PCN-224; (f) FT-IR of PB, PCN-224, PB-PCN-224; (g) N<sub>2</sub> adsorption—desorption isotherms of PCN-224 and PB-PCN-224. (For interpretation of the references to colour in this figure legend, the reader is referred to the web version of this article.)

impede the recombination of photogenerated electrons and holes.

The instantaneous photocurrent responses of the three materials were detected under 660 nm red light irradiation (Fig. 2c). When the light was on, a photocurrent was evident, but no response was observed in the dark, confirming that light was necessary for the generation of charge carriers. The photocurrent diagram showed that PB-PCN-224 had the highest photocurrent response of the three samples, confirming the fast charge separation between PB and PCN-224 and the low electron-hole pair recombination rate [44].

The negative scan of the linear sweep voltammetry (LSV) curve was showed in Fig. 2d. When compared with PB-PCN-224 in the dark, irradiated PB-PCN-224 showed a significant increase in photocurrent. This PB-PCN-224 photocurrent was also obviously larger than that of PB and PCN-224, thereby confirming the separation of electron-hole pairs in PB-PCN-224. Electrochemical impedance spectroscopy (EIS) measurements also indicated that PB-PCN-224 had the lowest impedance under illumination (Fig. 2e). This phenomenon verified that the PB-PCN-224 heterojunction had valid charge separation arising from a lessening of the recombination of electron-hole pairs. Taken together, these results further confirmed that PB-PCN-224 promoted photoelectron transfer and inhibited electron-hole pair recombination under 660 nm light irradiation.

In general, the plots of the Kubelka-Munk function versus the bandgap energy from the UV-visible diffuse reflectance spectra showed that the PCN-224 had a band gap of about 1.81 eV, while PB had a band gap of about 1.75 eV (Fig. S8). The conduction band (CB) and valence band (VB) (vs. Ag/AgCl) of PB were obtained as described previously [45]. The position of the CB of PCN-224 at -0.8 V vs. Ag/AgCl was

obtained from published work [46], and the VB of PCN-224 was calculated as 1.01 V vs. Ag/AgCl, associated with the tauc plot of PCN-224 (Fig. S8). The photocatalytic mechanism of PB-PCN-224 was summarized in Fig. 2f.

The band structure of PB-PCN-224 was a type II heterojunction. Under irradiation with 660 nm light, PB and PCN-224 were excited to generate electron-hole pairs. The different band gap widths of the two materials allowed separation of the generated electron-hole pairs and transferred between their CB and VB. Because the CB value was more negative for PB ( $-1.21~\rm V$  vs. Ag/AgCl) than for PCN-224 (-0.8 V vs. Ag/AgCl), the photo-generated electrons on the CB of PB could be transferred directly to the CB of PCN-224, and the residual  $h^+$  in the VB of PCN-224 was then shifted toward the VB of PB, thereby restraining the recombination of the photo-generated electron-hole pair. Since the recombination of the electron-hole pair of PCN-224 was effectively contained, the production of singlet oxygen in PB-PCN-224 would be significantly increased.

In the PB-PCN-224, only single oxygen was generated because hydroxyl radicals were generated under the condition where the VB position of the photocatalyst was higher than that of  $\rm H_2O/{}^{\bullet}OH$  pair (+1.99 V vs. NHE). By contrast, the VB position of the synthesized material was only 1.01 V vs. Ag/AgCl or 1.23 V vs. NHE, or significantly lower than that of  $\rm H_2O/{}^{\bullet}OH$  pair; therefore, hydroxyl radicals could not be generated [47,48]. Many literatures had also indicated that PB did not produce reactive oxygen species, while PCN-224 only produced singlet oxygen ( $^{1}O_{2}$ ) [49,50,46,51].

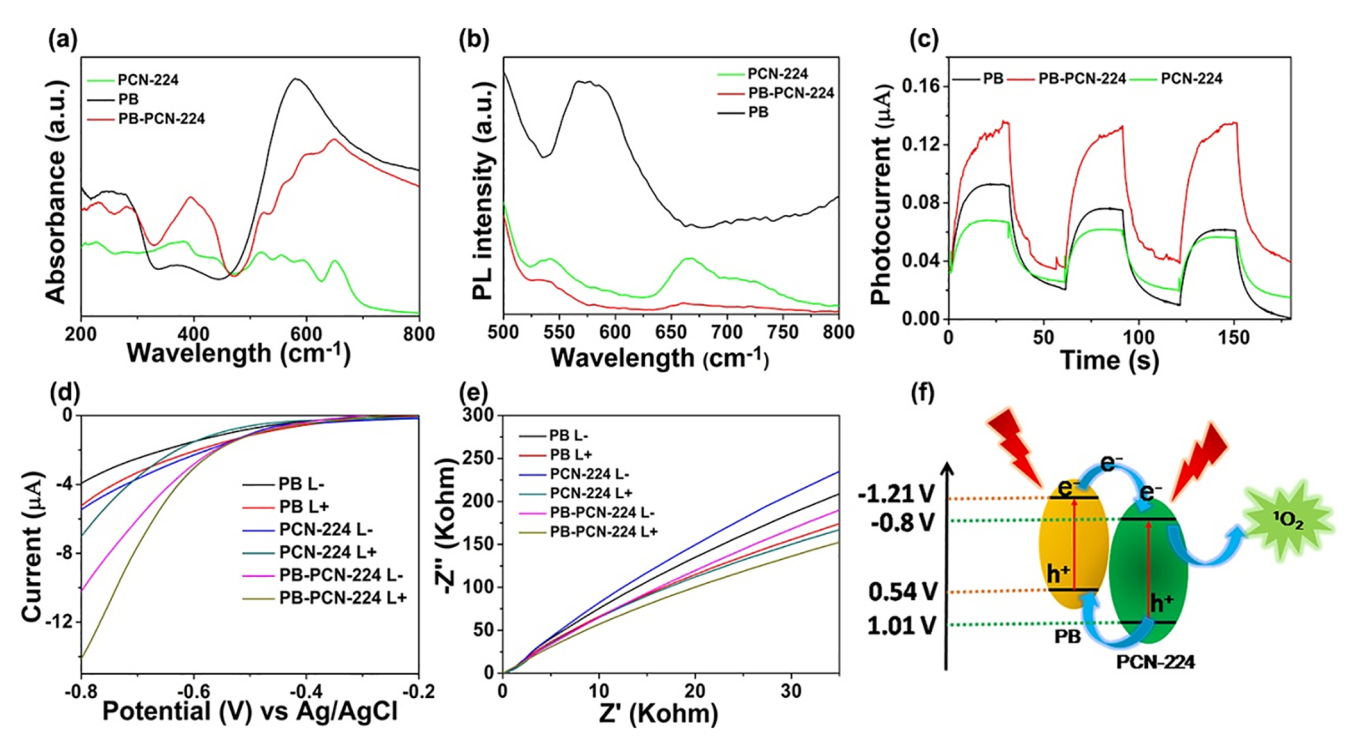


Fig. 2. (a) UV-visible diffuse reflection patterns of PB, PCN-224, and PB-PCN-224; (b) PL spectra of the materials with excitation wavelength of 420 nm; (c) Photocurrent spectra of PB, PCN-224, and PB-PCN-224 under 660 nm light irradiation; (d) LSV spectra of PB, PCN-224, and PB-PCN-224; (e) EIS spectra of PB, PCN-224, and PB-PCN-224; (f) Photocatalytic mechanism of the charge transfer for ROS evolution over the PB-PCN-224 under 660 nm light irradiation.

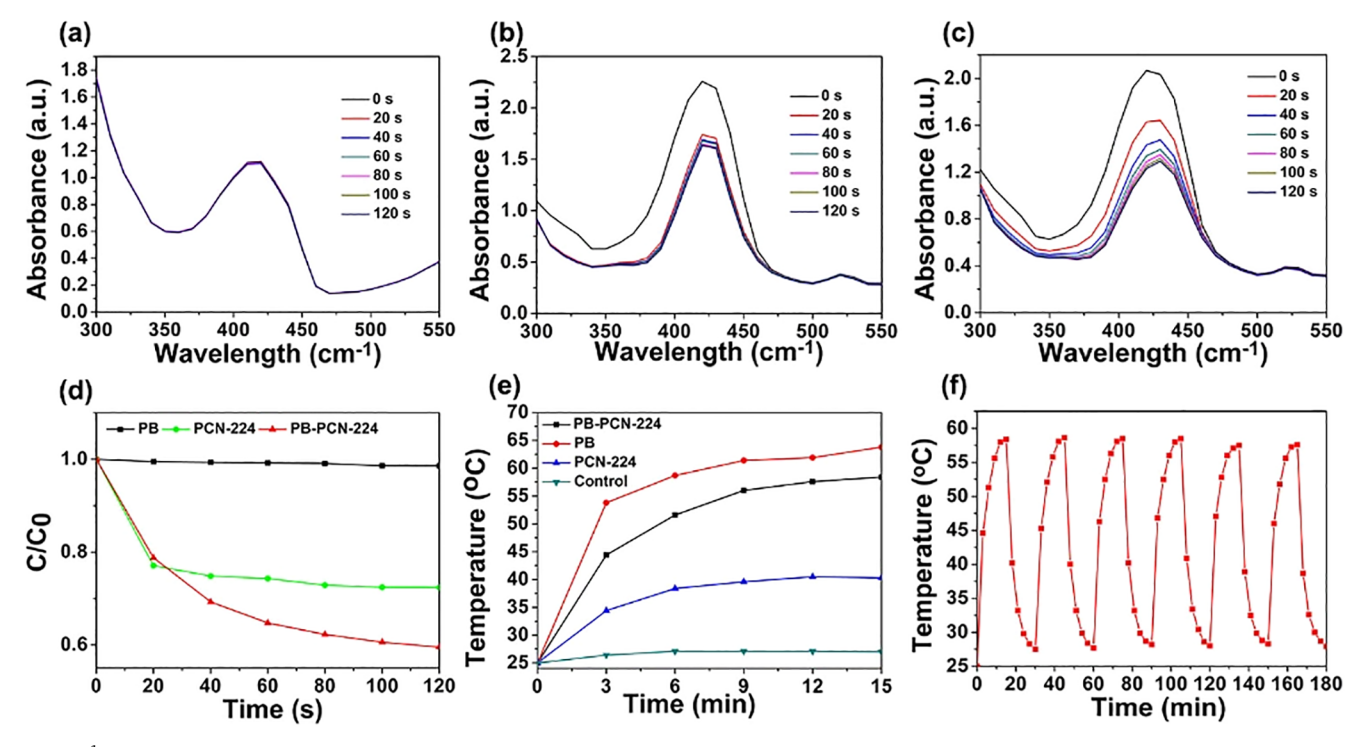
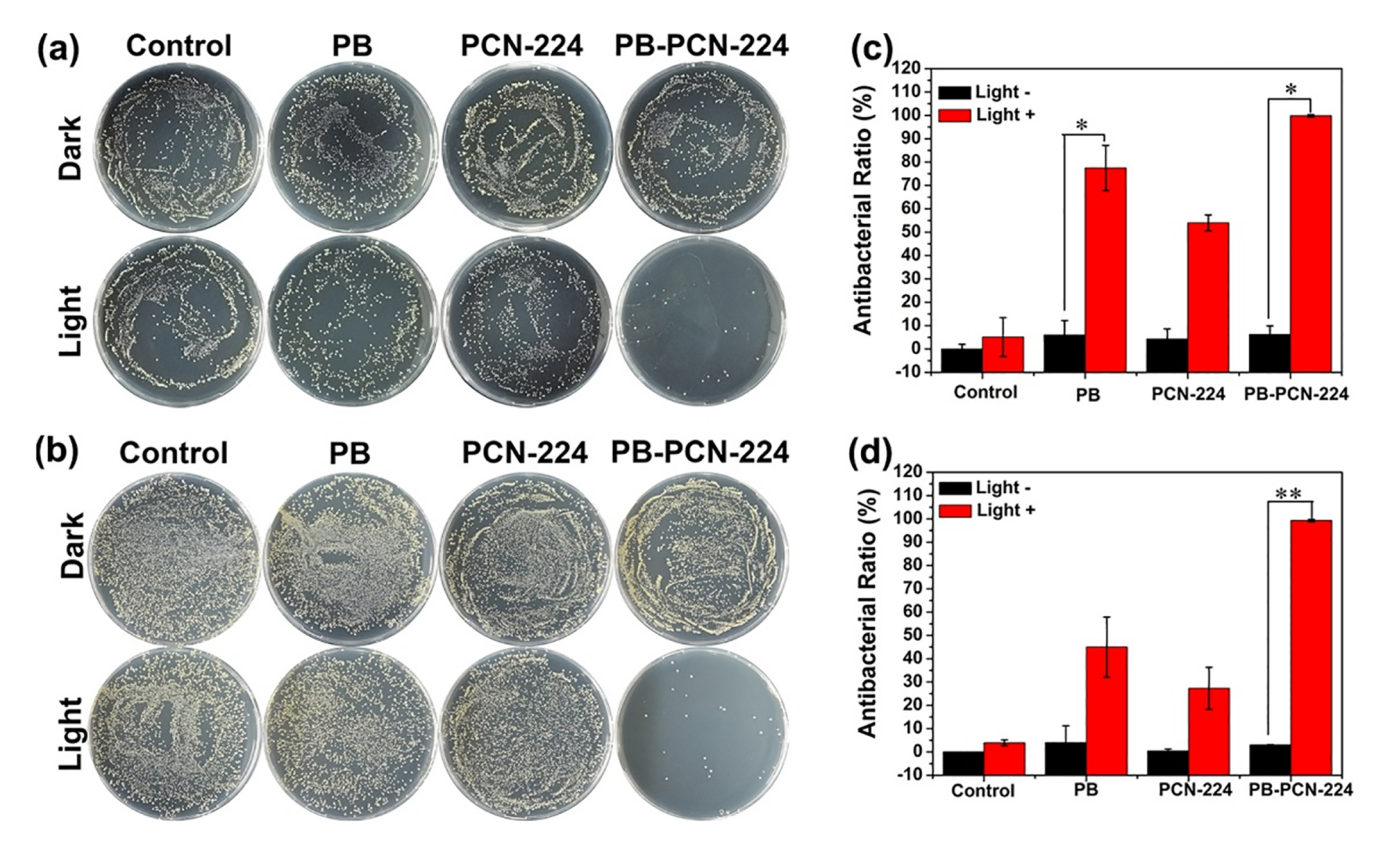


Fig. 3. The  $^{1}O_{2}$  detected through the reduction of DPBF of the materials under 660 nm light irradiation. (a) PB, (b) PCN-224, (c) PB-PCN-224; (d) The contrast curve between PB, PCN-224, and PB-PCN-224; (e) Photothermal heating curve of materials under 660 nm light irradiation; (f) Temperature heating and cooling curves of PB-PCN-224.

# 3.3. Photodynamic and photothermal characterization

The compound 1, 3-diphenyl isobenzofuran (DPBF) could be used as a  $^1\mathrm{O}_2$  collector, as it reacted with  $^1\mathrm{O}_2$  quickly to form a product with decreasing absorption strength at about 420 nm [52]. For the PB group, the UV absorption peak of DPBF solution was basically unchanged after

120 s exposure to 660 nm (0.3 W/cm<sup>2</sup>) (Fig. 3a). By contrast, the absorption intensity of PCN-224 and PB-PCN-224 under the irradiation of 660 nm light decreased gradually (Fig. 3b and c), indicating the generation of a large amount of  $^{1}O_{2}$ . At the same time, the generation of singlet oxygen only was consistent with previous literature reports [53,54]. Simultaneously, as shown in Fig. S9, the PCN-224 and PB-PCN-



**Fig. 4.** The spread plate images of (a) *S. aureus* and (b) *S. aureus* biofilm with the different materials with/without 660 nm light irradiation for 15 min; The antimicrobial ratios against (c) *S. aureus*, and (d) *S. aureus* biofilm according the spread plate pictures. Error bars indicate means  $\pm$  standard deviations: \*p < 0.05, \*\*p < 0.01.

224 had absorption at around 420 nm, but PB had no absorption at 420 nm. So after these three materials were mixed with DPBF, the UV absorption peak of DPBF at 0 s would be different. As shown in Fig. S10, the absorption of DPBF was basically unchanged under the dark condition, indicating that the decline of DPBF absorption was dependent on the production of reactive oxygen species by the photoactivated material rather than the adsorption by the material itself. However, the ROS yield of PCN-224 was smaller than that of PB-PCN-224 (Fig. 3d), reflecting the effect of the heterojunction between PB and PCN-224, which expedited the shift and separation rate of photogenic electronhole pairs that were conducive to the generation of ROS (Fig. 2). At the same time, we also synthesized PCN-224 doped with different amounts of PB, which were 5-PB-PCN-224, 10-PB-PCN-224 (that was, PB-PCN-224), and we also tested their ability to generate active oxygen. It was found that with the increase of PB doping, its ability to produce active oxygen also increased (Fig. S11). The electron spin resonance (ESR) spectra of MOF was detected. The 2, 2, 6, 6-Tetramethylpiperidine (TEMP) was used as a singlet oxygen capture agent [55], but the TEMP solution was strongly alkaline, and PB would dissolve under alkaline conditions. The UV-visible absorption spectrum of PB showed that PB would be decomposed no matter it was under light or dark conditions, so ESR cannot be used to measure the singlet oxygen of the material (Fig. S12). As shown in Fig. S13, 5,5-dimethyl-1-pyrroline-N-oxide (DMPO, 0.1 mol/L) was used as a capture agent for hydroxyl radical (•OH) [56], no matter what kind of material (PB, PCN-224, PB- PCN-224) would not produce hydroxyl radicals.

PB-PCN-224 had strong absorption intensity in the range of 500–800 nm (Fig. 2a), so it might have a good photothermal effect under 660 nm light irradiation. The heating temperature curve of the sample was shown in Fig. 3e. The sample was irradiated with 660 nm light for 15 min  $(0.3 \text{ W/cm}^2)$ . After 6 min of irradiation, the surface temperatures of PB and PB-PCN-224 increased to  $58.7 \,^{\circ}$ C and  $51.6 \,^{\circ}$ C, respectively. By contrast, under the same condition, the temperature of

PCN-224 only increased to 38.4 °C, indicating that PB was the main source of photo-induced hyperthermia.

Fig. S14 shows the real-time photothermal image curves corresponding to Fig. 3e. As shown in Fig. 3f, the photothermal stability of PB-PCN-224 under 660 nm light irradiation was determined by studying on–off cycles of the laser during the illumination of PB-PCN-224. Stable temperature variations and almost unaltered maximal temperatures were observed, which verified the excellent photothermal stability of PB-PCN-224.

# 3.4. Antibacterial test

A plate coating method was used to show the antibacterial effect of the materials. The antibacterial rate was determined directly from the number of bacterial colonies. The PBS group (control group) showed many bacterial colonies following 660 nm red light illumination or a dark treatment for 15 min, indicating that 15 min of light exposure had no effect on bacterial viability (Fig. 4a and 4b). Obviously, the PB and PCN-224 groups had low antibacterial efficiency against S. aureus (77.47% and 54%, respectively, Fig. 4c) and S. aureus biofilm (45% and 27.33%, respectively, Fig. 4d). By contrast, the PB-PCN-224 group showed excellent antibacterial properties after 15 min irradiation in 660 nm red light, as only a few bacterial colonies were present on plate. The corresponding antibacterial efficiency against S. aureus and its biofilm was 99.84% (Fig. 4c) and 99.30% (Fig. 4d), respectively, which indicated that PB-PCN-224 could rapidly kill bacteria under 660 nm light irradiation for 15 min. These results also showed that PTT alone was more effective than PDT alone, as demonstrated by the diffusion plate results for the PB and PCN-224 groups. Therefore, a single model incorporating PTT or PDT antibacterial processes did not completely and effectively eradicate bacteria. The antibacterial effect against S. aureus was higher with the combination of PTT and PDT than with PTT or PDT alone. In addition, we also summarized the latest antibacterial

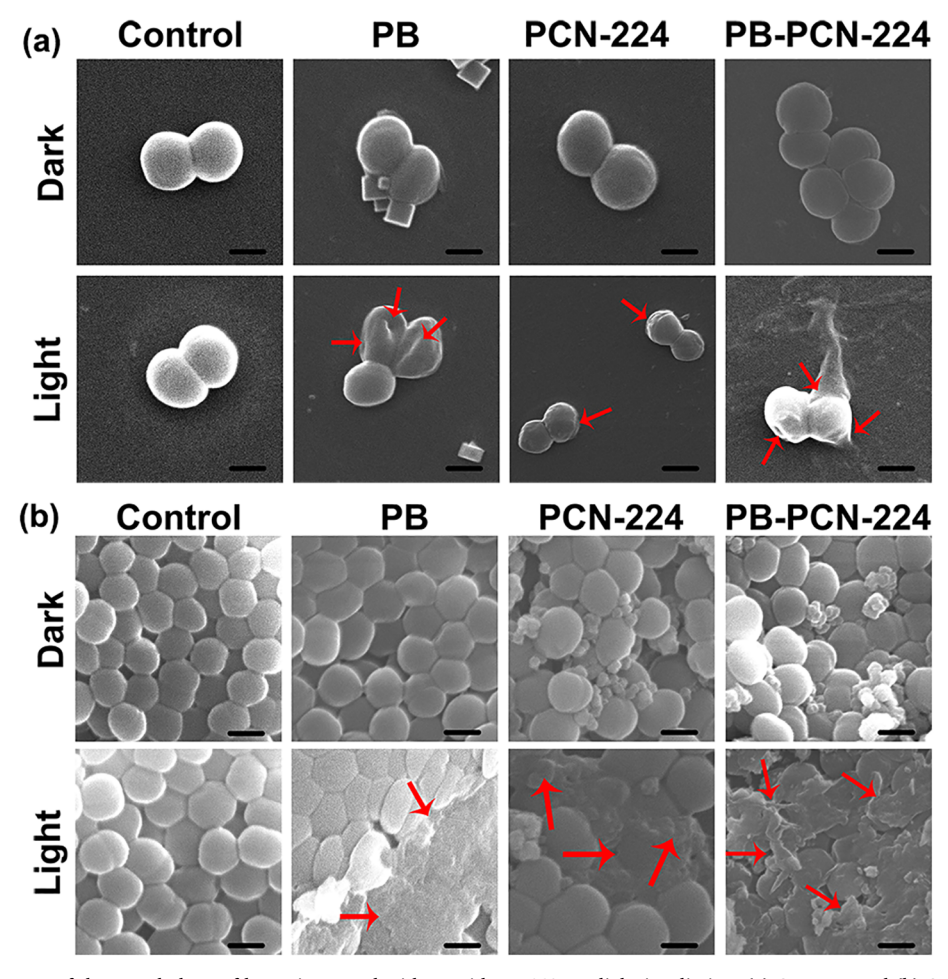


Fig. 5. SEM pictures of the morphology of bacteria treated with or without 660 nm light irradiation. (a) S. aureus and (b) S. aureus biofilm.

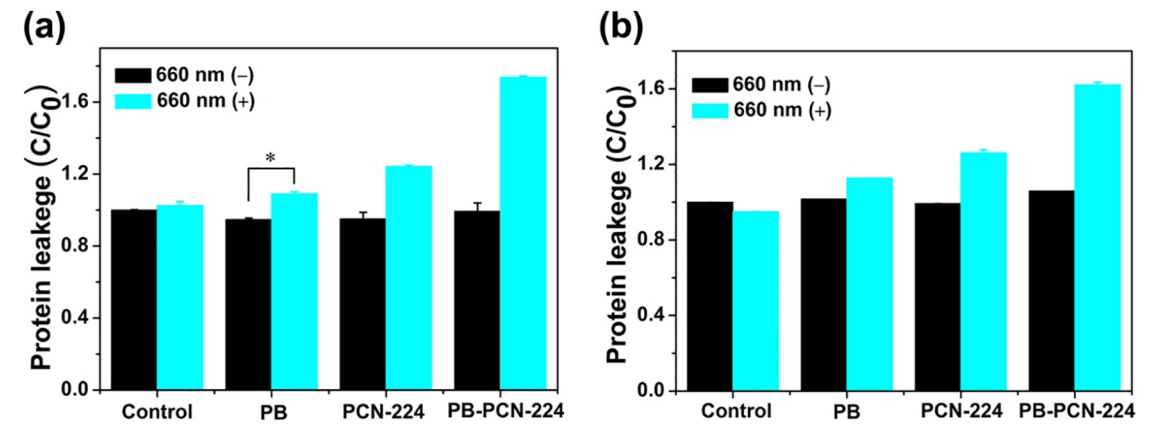


Fig. 6. The protein leakage concentration for the bacteria treated or not treated with 660 nm light irradiation (a) S. aureus and (b) S. aureus biofilms. \*P < 0.05.

literature and found that photothermal and photodynamics were widely used in antibacterial research (Table S1).

We also explored whether the structure of the material was changed before or after antibacterial test. As shown in Fig. S15, the morphology and structure of the material before and after the antibacterial tests were essentially unchanged, indicating that the material had good antibacterial stability.

*S. aureus* and its biofilms, when cultured with the control group, showed normal morphology with a smooth and complete surface following the treatment of light irradiation or in the dark (Fig. 5a and 5b), showing that the PBS had no bacteriostatic effects under light

condition. The bacterial membranes of all samples remained intact and smooth under the dark conditions, indicating that none of the samples had significant antibacterial activity in the dark. As a contrast, in the PB and PCN-224 treatment groups, *S. aureus* showed varying degrees of deformation after 15 min of exposure to 660 nm light, as revealed by membrane damage of the cultured bacteria. More severe membrane contraction and even rupture were observed in the bacteria in the PB-PCN-224 group (red arrow).

The viability of the bacteria was assessed by the live/dead (green/red) staining assay. As shown in Fig. S16, when there was no light irradiation, most of the fluorescent images were green, indicating that

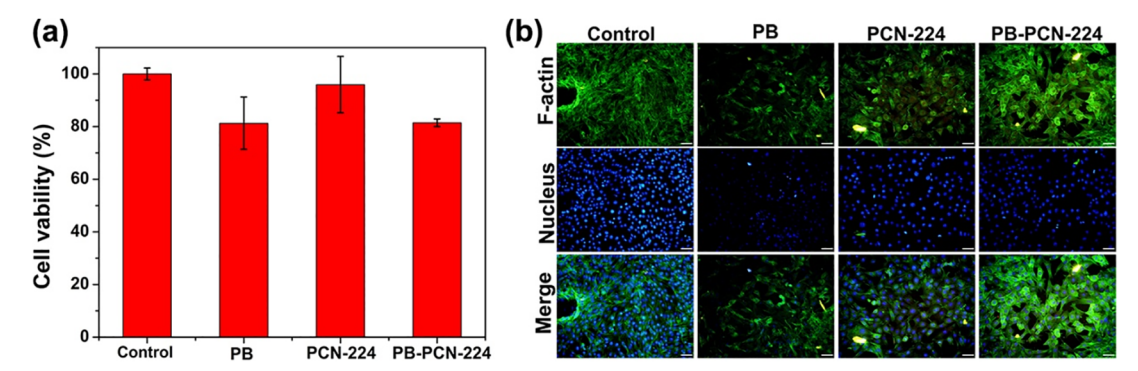


Fig. 7. (a) The cell viability of different samples after cultivated for 1 day was detected by MTT assay; (b) Fluorescence images of NIH-3 T3 cells co-cultured with different samples for 24 h. The cytoplasm were stained with FITC (green) and the nuclei were stained with DAPI (blue), scale bare = 100 μm. (For interpretation of the references to colour in this figure legend, the reader is referred to the web version of this article.)

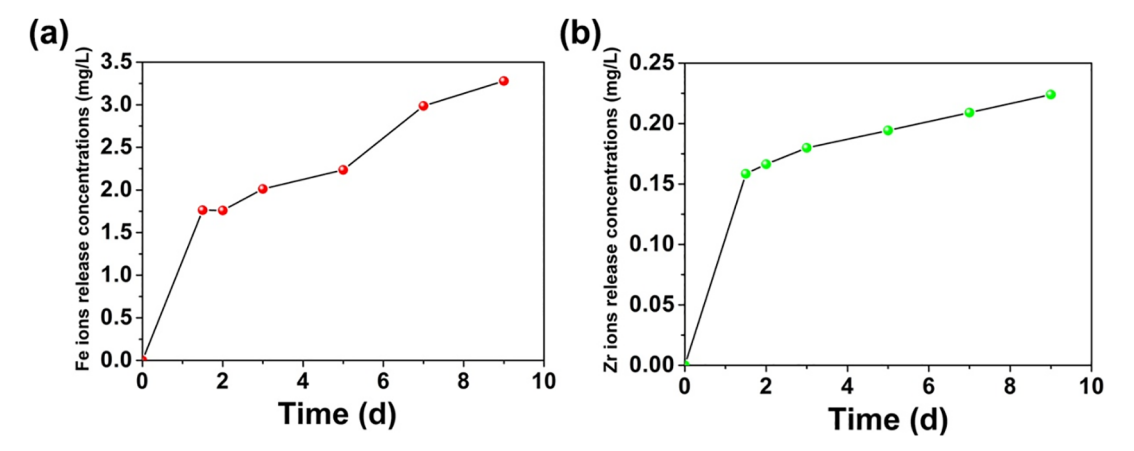


Fig. 8. The ion release concentration from PB-PCN-224. (a) Fe ions, and (b) Zr ions.

the material itself had no bactericidal effect. After irradiating with 660 nm light for 15 min, part of the red fluorescence appeared in the PB and PCN-224 groups, while PB-PCN-224 basically had no green fluorescence, indicating that under the synergistic effect of ROS and photothermal, PB-PCN-224 had a good antibacterial effect. The live/dead analysis results were consistent with the plate coating results. DCFH-DA was used to measure intracellular ROS, and ROS detection assay was done via fluorescence microscopic method. As shown in Fig. S17, in dark conditions, ROS were not produced in bacteria. After illumination for 15 min, the bacteria in PB group, PCN-224 group and PB-PCN-224 group all showed green fluorescence, among which PB-PCN-224 group showed the brightest green fluorescence, indicating that the bacteria produced more ROS.

In summary, these findings suggested that the synergistic effect of PTT and PDT was responsible for effective sterilization in a short time. As shown in Fig. 6a and 6b, the protein leakage level of bacteria in the PB and PCN-224 group was about 1.1–1.3 times that of the control group after 660 nm light irradiation for 15 min. This confirmed that the membrane of bacteria in the two groups was weakened by the sterilization process under 660 nm light irradiation, in agreement with the spread plate results (Fig. 4) and the morphological observation (Fig. 5). In contrast, the greatest protein leakage was seen for the PB-PCN-224 group, at 1.7 times and 1.6 times higher than the one in the control groups, respectively, indicating that PB-PCN-224 effectively killed bacteria by severely destroying their membranes and the subsequent proteins leakage under 660 nm light illumination for 15 min.

# 3.5. Cytotoxicity test

Cytotoxicity was measured by MTT experiments. After one day of treatment, the cell viability of the PB, PCN-224 and PB-PCN-224 groups

was 81.29%, 95.96% and 81.45%, respectively, when compared with the control group (Fig. 7a). The MTT data confirmed that none of the samples were significantly cytotoxic and that PB and PCN-224 had excellent biocompatibility. Further cytotoxicity assessment of the samples by fluorescence staining to observe the cell morphology confirmed that all the cells showed spindle proliferation morphology and showed polygons with filamentous pseudopods and lamellar liposome (Fig. 7b). This might be because the porous structure and large specific surface area of MOF could provide more active sites, so that the filamentous pseudopods of the cell had more anchoring points, which was conducive to the adhesion and proliferation of cells. At the same time, iron ions and zirconium ions released from PB-PCN-224 were metal ions with low toxicity and good biocompatibility (Fig. 8a and b), and iron ions could promote cell differentiation through the secretion of collagen [57,58,59], so the material had good biocompatibility.

# 3.6. Animal experiment

The course of wound healing in the rat wound model at different time points were showed in Fig. S18. The wounds were distinctly smaller in the experimental group treated with PB-PCN-224 than in the other groups after 8 days of therapy. During the experiment, after two days of treatment, all groups showed severe bacterial infections, as revealed by Giemsa staining (Fig. 9a, red arrows). The numbers of attached bacteria around the wound were much lower in the test group treated with PB-PCN-224 than in the control and 3 M groups. The number of neutrophils in the soft tissue also indicated bacterial infection, as neutrophils rapidly migrate from the circulating blood to the sites of infection in response to infection. As shown in Fig. 9b, H&E staining revealed a number of segmented neutrophils (red arrows) around the wound, indicating severe bacterial infection. This infection

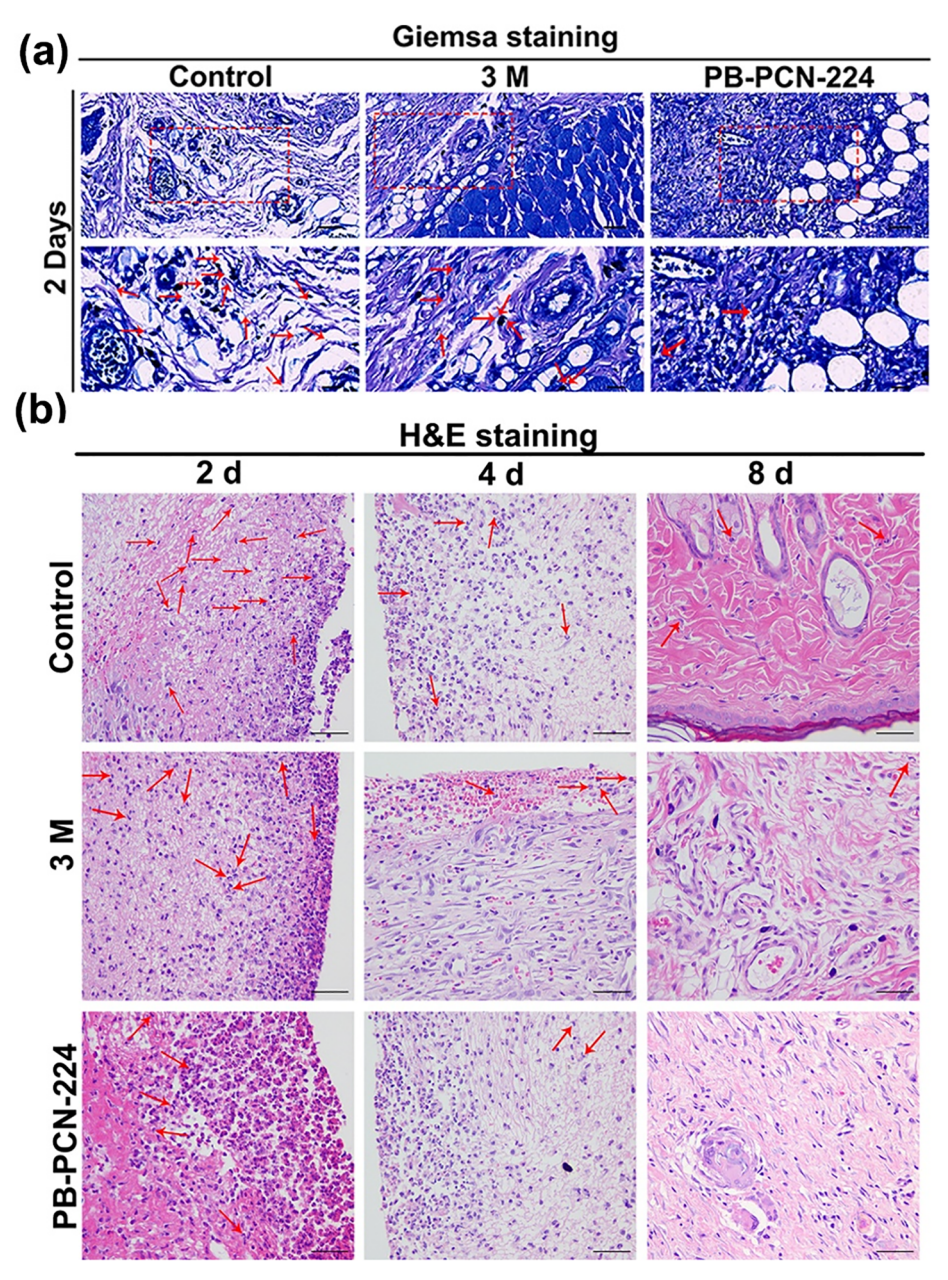


Fig. 9. (a) The wound tissue stained with Giemsa after 2 days of therapy; (b) The degree of infection of the wound tissue at 2, 4 and 8 days was revealed by H&E staining. Scale bars, 50 nm.

was particularly evident in the 3 M and control groups during the first 4 days. By contrast, the number of neutrophils in the test group was small, and most of the cells were normal, suggesting a relatively small infection and confirming the strong antibacterial activity of PB-PCN-244. Histological analysis of the major organs (heart, liver, spleen, lung and kidney), as shown in Fig. S19, did not reveal any aberrant structures or injuries after 8 days of therapy, suggesting that materials were safe for *in vivo* use.

# 4. Conclusion

PB-PCN-224 with photothermal and photodynamic effects was designed and manufactured. The biomaterial had 99.84% and 99.3% effective against *S. aureus* and its biofilm under irradiation with 660 nm light. PB-PCN-224 had no obvious biological toxicity. In conclusion, the combinations of synergistic antibacterial materials appear to be promising methods for sterilization without adverse side effects.

# **Declaration of Competing Interest**

The authors declare that they have no known competing financial interests or personal relationships that could have appeared to influence the work reported in this paper.

# Acknowledgments

This work is jointly supported by the National Science Fund for Distinguished Young Scholars 51925104, National Natural Science Foundation of China nos. 51871162, and 51671081, 81870809, the National Key Research and Development Program of China 2016YFC1100600 (subproject 2016YFC1100604), Natural Science Fund of Hubei Province, 2018CFA064, RGC/NSFC (N\_HKU725-1616), Hong Kong ITC (ITS/287/17, GHX/002/14SZ), as well as Health and Medical Research Fund (No. 03142446), NSFC 51925104.

## Appendix A. Supplementary data

Supplementary data to this article can be found online at https://doi.org/10.1016/j.cej.2020.126730.

#### References

- S. Schreml, R.M. Szeimies, L. Prantl, S. Karrer, M. Landthaler, P. Babilas, Oxygen in acute and chronic wound healing, Br. J. Dermatol. 163 (2010) 257–268.
- [2] Z. Xie, C.B. Paras, H. Weng, P. Punnakitikashem, L.C. Su, K. Vu, L. Tang, J. Yang, K.T. Nguyen, Dual growth factor releasing multi-functional nanofibers for wound healing, Acta Biomater. 9 (2013) 9351–9359.
- [3] C. Mao, Y. Xiang, X. Liu, Z. Cui, X. Yang, Z. Li, S. Zhu, Y. Zheng, K.W.K. Yeung, S. Wu, Repeatable photodynamic therapy with triggered signaling pathways of fibroblast cell proliferation and differentiation to promote bacteria-accompanied wound healing, ACS Nano 12 (2018) 1747–1759.
- [4] X. Zhang, G. Zhang, H. Zhang, X. Liu, J. Shi, H. Shi, X. Yao, P.K. Chu, X. Zhang, A bifunctional hydrogel incorporated with CuS@MoS<sub>2</sub> microspheres for disinfection and improved wound healing, Chem. Eng. J. 382 (2020) 122849.
- [5] E.L. Zhang, S. Fu, R.X. Wang, H.X. Li, Y. Liu, Z.Q. Ma, G.K. Liu, C.S. Zhu, G.W. Qin, D.F. Chen, Role of Cu element in biomedical metal alloy design, Rare Met. 36 (2019) 476–494.
- [6] J.M. Zhang, Y.H. Sun, Y. Zhao, Y.L. Liu, X.H. Yao, B. Tang, R.Q. Hang, Antibacterial ability and cytocompatibility of Cu-incorporated Ni–Ti–O nanopores on NiTi alloy, Rare Met. 36 (2019) 552–560.
- [7] Z. Miao, L. Fan, X. Xie, Y. Ma, J. Xue, T. He, Z. Zha, Liquid exfoliation of atomically thin antimony selenide as an efficient two-dimensional antibacterial nanoagent, ACS Appl. Mater. Interfaces 11 (2019) 26664–26673.
- [8] Y.S. Huang, H.H. Huang, Effects of clinical dental implant abutment materials and their surface characteristics on initial bacterial adhesion, Rare Met. 36 (2019) 512–519.
- [9] L. Wang, X. Zhang, X. Yu, F. Gao, Z. Shen, X. Zhang, S. Ge, J. Liu, Z. Gu, C. Chen, An all-organic semiconductor C<sub>3</sub>N<sub>4</sub>/PDINH heterostructure with advanced antibacterial photocatalytic therapy activity, Adv. Mater. 31 (2019) 1901965.
- [10] J. Xing, S. Qi, Z. Wang, X. Yi, Z. Zhou, J. Chen, S. Huang, G. Tan, D. Chen, P. Yu, C. Ning, Antimicrobial peptide functionalized conductive nanowire array electrode as a promising candidate for bacterial environment application, Adv. Funct. Mater. 29 (2019) 1806353.
- [11] K. Quan, Z. Zhang, H. Chen, X. Ren, Y. Ren, B.W. Peterson, H.C. van der Mei, H.J. Busscher, Artificial channels in an infectious biofilm created by magnetic nanoparticles enhanced bacterial killing by antibiotics, Small 15 (2019) 1902313.
- [12] Y. Wu, Z. Song, H. Wang, H. Han, Endogenous stimulus-powered antibiotic release from nanoreactors for a combination therapy of bacterial infections, Nat. Commun. 10 (2019) 4464.
- [13] V.M. D'Costa, C.E. King, L. Kalan, M. Morar, W.W.L. Sung, C. Schwarz, D. Froese, G. Zazula, F. Calmels, R. Debruyne, G.B. Golding, H.N. Poinar, G.D. Wright, Antibiotic resistance is ancient, Nature 477 (2011) 457–461.
- [14] B. Huang, L. Tan, X. Liu, J. Li, S. Wu, A facile fabrication of novel stuff with anti-bacterial property and osteogenic promotion utilizing red phosphorus and near-infrared light, Bioact. Mater. 4 (2019) 17–21.
- [15] M. Wang, K. Deng, W. Lü, X. Deng, K. Li, Y. Shi, B. Ding, Z. Cheng, B. Xing, G. Han, Z. Hou, J. Lin, Rational design of multifunctional Fe@γ-Fe<sub>2</sub>O<sub>3</sub>@H-TiO<sub>2</sub> nanocomposites with enhanced magnetic and photoconversion effects for wide applications: from photocatalysis to imaging-guided photothermal cancer therapy, Adv. Mater. 30 (2018) 1706747.
- [16] M. Chang, M. Wang, M. Wang, M. Shu, B. Ding, C. Li, M. Pang, S. Cui, Z. Hou, J. Lin, A multifunctional cascade bioreactor based on hollow-structured Cu<sub>2</sub>MoS<sub>4</sub> for synergetic cancer chemo-dynamic therapy/starvation therapy/phototherapy/immunotherapy with remarkably enhanced efficacy, Adv. Mater, 31 (2019) 1905271.
- [17] X. Zhang, C. Zhang, Y. Yang, H. Zhang, X. Huang, R. Hang, X. Yao, Light-assisted rapid sterilization by a hydrogel incorporated with Ag<sub>3</sub>PO<sub>4</sub>/MoS<sub>2</sub> composites for efficient wound disinfection, Chem. Eng. J. 374 (2019) 596–604.
- [18] J. Li, X. Liu, L. Tan, Z. Cui, X. Yang, Y. Liang, Z. Li, S. Zhu, Y. Zheng, K.W.K. Yeung, X. Wang, S. Wu, Zinc-doped Prussian blue enhances photothermalclearance of Staphylococcus aureus and promotestissue repair in infected wounds, Nat. Commun. 10 (2019) 4490.
- [19] Z. Zhou, J. Song, L. Nie, X. Chen, Reactive oxygen species generating systems meeting challenges of photodynamic cancer therapy, Chem. Soc. Rev. 45 (2016) 6597–6626.
- [20] J. Kennedy, I.S. Blair, D.A. McDowell, D.J. Bolton, An investigation of the thermal inactivation of Staphylococcus aureus and the potential for increased thermotolerance as a result of chilled storage, J. Appl. Microbiol. 99 (2005) 1229–1235.
- [21] W. Wang, X. Cheng, J. Liao, Z. Lin, L. Chen, D. Liu, T. Zhang, L. Li, Y. Lu, H. Xia, Synergistic photothermal and photodynamic therapy for effective implant-related bacterial infection elimination and biofilm disruption using <sub>C</sub>u<sub>9</sub>S8 nanoparticles, ACS Biomater. Sci. Eng. 5 (2019) 6243–6253.
- [22] M. Li, L. Li, K. Su, X. Liu, T. Zhang, Y. Liang, D. Jing, X. Yang, D. Zheng, Z. Cui, Z. Li, S. Zhu, K.W.K. Yeung, Y. Zheng, X. Wang, S. Wu, Highly effective and noninvasive near-infrared eradication of a staphylococcus aureus biofilm on implants by a photoresponsive coating within 20 Min, Adv. Sci. 6 (2019) 1900599.
- [23] L. Jiao, Y. Wang, H.L. Jiang, Q. Xu, Metal-organic frameworks as platforms for catalytic applications, Adv. Mater. 30 (2018) 1703663.
   [24] P. Li, Y. Shen, D. Wang, Y. Chen, Y. Zhao, Selective adsorption-based separation of
- [24] P. Li, Y. Shen, D. Wang, Y. Chen, Y. Zhao, Selective adsorption-based separation of flue gas and natural gas in zirconium metal-organic frameworks nanocrystals,

- Molecules 24 (2019)
- [25] J.S. Kahn, L. Freage, N. Enkin, M.A.A. Garcia, I. Willner, Stimuli-responsive DNA-functionalized metal-organic frameworks (MOFs), Adv. Mater. 29 (2017) 1602782.
- [26] R. Zhu, J. Ding, Y. Xu, J. Yang, Q. Xu, H. Pang, π-Conjugated molecule boosts metal–organic frameworks as efficient oxygen evolution reaction catalysts, Small 14 (2018) 1803576.
- [27] Y. Shi, A.F. Yang, C.S. Cao, B. Zhao, Applications of MOFs: recent advances in photocatalytic hydrogen production from water, Coord. Chem. Rev. 390 (2019) 50–75
- [28] M. Alvaro, E. Carbonell, B. Ferrer, F.X.L.i. Xamena, H. Garcia, Semiconductor behavior of a metal-organic framework (MOF), Chem. Eur. J. 13 (2007) 5106–5112.
- [29] K.G.M. Laurier, F. Vermoortele, R.P. Ameloot, D.D. Vos, J. Hofkens, M.B.J. Roeffaers, Iron(III)-based metal-organic frameworks as visible light photocatalysts, J. Am. Chem. Soc. 135 (2013) 14488–14491.
- [30] A. Dhakshinamoorthy, A.M. Asiri, H. Garcia, Metal-organic framework (MOF) compounds: photocatalysts for redox reactions and solar fuel production, Angew. Chem. Int. Ed. 55 (2016) 5414–5445.
- [31] W.Y. Gao, M. Chrzanowski, S. Ma, Metal-metalloporphyrin frameworks: a resurging class of functional materials, Chem. Soc. Rev. 43 (2014) 5841–5866.
- [32] T. He, S. Chen, B. Ni, Y. Gong, Z. Wu, L. Song, L. Gu, W. Hu, X. Wang, Zirconium-porphyrin based metal-organic framework hollow nanotubes for immobilization of noble metal single atoms, Angew. Chem. Int. Ed. 57 (2018) 3493–3498.
- [33] X. Li, Y. Pi, Q. Xia, Z. Li, J. Xiao, TiO<sub>2</sub> encapsulated in salicylaldehyde-NH<sub>2</sub>-MIL-101(Cr) for enhanced visible light-driven photodegradation of MB, Appl. Catal.B-Environ. 191 (2016) 192–201.
- [34] C. Zhang, Y. Xu, M. Zhou, L. Liang, H. Dong, M. Wu, Y. Yang, Y. Lei, Potassium prussian blue nanoparticles: a low-cost cathode material for potassium-ion batteries, Adv. Funct. Mater. 27 (2017) 1604307.
- [35] D. Wang, J. Zhou, R. Chen, R. Shi, G. Zhao, G. Xia, R. Li, Z. Liu, J. Tian, H. Wang, Z. Guo, H. Wang, Q. Chen, Controllable synthesis of dual-MOFs nanostructures for pH-responsive artemisinin delivery, magnetic resonance and optical dual-model imaging-guided chemo/photothermal combinational cancer therapy, Biomaterials 100 (2016) 27–40.
- [36] J. Wang, Y. Fan, Y. Tan, X. Zhao, Y. Zhang, C. Cheng, M. Yang, Porphyrinic metalorganic framework PCN-224 nanoparticles for near-IR induced attenuation of aggregation and neurotoxicity of alzheimer's amyloid-# peptide, ACS Appl. Mater. Interfaces 10 (2018) 36615–36621.
- [37] M. Jahan, Q. Bao, K.P. Loh, Electrocatalytically active graphene porphyrin MOF composite for oxygen reduction reaction, J. Am. Chem. Soc. 134 (2012) 6707–6713.
- [38] H. Hu, W. Liu, M. Zhu, Y. Lin, Y. Liu, J. Zhang, T. Chen, K. Liu, Yolk-shell prussian blue nanoparticles with fast ion diffusion for sodium-ion battery, Mater. Lett. 249 (2019) 206–209.
- [39] G. Yilmaz, C.F. Tan, M. Hong, G.W. Ho, Functional defective metal-organic coordinated network of mesostructured nanoframes for enhanced electrocatalysis, Adv. Funct. Mater. 28 (2018) 1704177.
- [40] H. Zhang, J. Wei, J. Dong, G. Liu, L. Shi, P. An, G. Zhao, J. Kong, X. Wang, X. Meng, J. Zhang, J. Ye, Efficient visible-light-driven carbon dioxide reduction by a singleatom implanted metal-organic framework, Angew. Chem. Int. Ed. 55 (2016) 14310-14314.
- [41] L. Cao, Y. Liu, B. Zhang, L. Lu, In situ controllable growth of Prussian blue nanocubes on reduced graphene oxide: facile synthesis and their application as enhanced nanoelectrocatalyst for H2O2 reduction, ACS Appl. Mater. Interfaces 2 (2010) 2339–2346.
- [42] M. Peng, G. Guan, H. Deng, B. Han, C. Tian, J. Zhuang, Y. Xu, W. Liu, Z. Lin, PCN-224/rGO nanocomposite based photoelectrochemical sensor with intrinsic recognition ability for efficient p-arsanilic acid detection, Environ. Sci.: Nano 6 (2019) 207–215.
- [43] J.D. Xiao, Q. Shang, Y. Xiong, Q. Zhang, Y. Luo, S.H. Yu, H. Jiang, Boosting photocatalytic hydrogen production of a metal-organic framework decorated with platinum nanoparticles: the platinum location matters, Angew. Chem. Int. Ed. 55 (2016) 9389–9393.
- [44] J. Xi, H. Xia, X. Ning, Z. Zhang, J. Liu, Z. Mu, S. Zhang, P. Du, X. Lu, Carbon-intercalated 0D/2D hybrid of hematite quantum dots/graphitic carbon nitride nanosheets as superior catalyst for advanced oxidation, Small 1902744 (2019).
- [45] Y. Luo, J. Li, X. Liu, L. Tan, Z. Cui, X. Feng, X. Yang, Y. Liang, Z. Li, S. Zhu, Y. Zheng, K.W.K. Yeung, C. Yang, X. Wang, S. Wu, Dual metal – organic framework heterointerface, ACS Cent. Sci. 5 (2019) 1591–1601.
- [46] Y.Z. Chen, Z.U. Wang, H. Wang, J. Lu, S.H. Yu, H.L. Jiang, Singlet oxygen-engaged selective photo-oxidation over Pt nanocrystals/porphyrinic MOF: the roles of photothermal effect and Pt electronic state, J. Am. Chem. Soc. 139 (2017) 2035–2044.
- [47] J. Qiu, W. Zheng, R. Yuan, C. Yue, D. Li, F. Liu, J. Zhu, A novel 3D nanofibrous aerogel-based  $MoS_2@Co_3S_4$  heterojunction photocatalyst for water remediation and hydrogen evolution under simulated solar irradiation, Appl. Catal. B-Environ. 264 (2020) 118514.
- [48] M. Xiong, L. Chen, Q. Yuen, J. He, S.L. Luo, C.T. Au, S.F. Yin, Controlled synthesis of graphitic carbon nitride/beta bismuth oxide composite and its high visible-light photocatalytic activity, Carbon 86 (2015) 217–224.
- [49] R. Yang, M. Hou, Y. Gao, L. Zhang, Z. Xu, Y. Kang, P. Xue, Indocyanine green-modified hollow mesoporous prussian blue nanoparticles loading doxorubicin for fluorescence-guided tri-modal combination therapy of cancer, Nanoscale 11 (2019) 5717–5731.
- [50] Z.L. Yang, W. Tian, Q. Wang, Y. Zhao, Y.L. Zhang, Y. Tian, Y.X. Tang, S.J. Wang, Y. Liu, Q.Q. Ni, G.M. Lu, Z.G. Teng, L.J. Zhang, Oxygen-evolving mesoporous organosilica coated Prussian blue nanoplatform for highly efficient photodynamic therapy of tumors, Adv. Sci. 5 (2018) 1700847.

- [51] J.Y. Zeng, M.K. Zhang, M.Y. Peng, D. Gong, X.Z. Zhang, Porphyrinic metal-organic frameworks coated gold nanorods as a versatile nanoplatform for combined photodynamic/photothermal/chemotherapy of tumor, Adv. Funct. Mater. 28 (2018) 1705451.
- [52] H. Wang, X. Yang, W. Shao, S. Chen, J. Xie, X. Zhang, J. Wang, Y. Xie, Ultrathin black phosphorus nanosheets for efficient singlet oxygen generation, J. Am. Chem. Soc. 135 (2015) 11376–11382.
- [53] Y. Zhang, F. Wang, C. Liu, Z. Wang, L. Kang, Y. Huang, K. Dong, J. Ren, X. Qu, Nanozyme decorated metal–organic frameworks for enhanced photodynamic therapy, ACS Nano 12 (2018) 651–661.
- [54] Y. Ding, Y.P. Chen, X. Zhang, L. Chen, Z. Dong, H.L. Jiang, H. Xu, H.C. Zhou, Controlled intercalation and chemical exfoliation of layered metal-organic frameworks using a chemically labile intercalating agent, J. Am. Chem. Soc. 139 (2017) 9136-9130
- [55] W. He, H.K. Kim, W.G. Wamer, D. Melka, J.H. Callahan, J.J. Yin, Photogenerated

- charge carriers and reactive oxygen species in ZnO/Au hybrid nanostructures with enhanced photocatalytic and antibacterial activity, J. Am. Chem. Soc. 136 (2014) 750–757.
- [56] D.F. Laine, A. Blumenfeld, I.F. Cheng, Mechanistic study of the ZEA organic pollutant degradation system: evidence for H<sub>2</sub>O<sub>2</sub>, HO+, and the homogeneous activation of O<sub>2</sub> by Fe<sup>II</sup>EDTA, Ind. Eng. Chem. Res. 47 (2008) 6502–6508.
- [57] E.S. Jang, J.H. Shin, G. Ren, M.J. Park, K. Cheng, X. Chen, J.C. Wu, J.B. Sunwoo, Z. Cheng, The manipulation of natural killer cells to target tumor sites using magnetic nanoparticles, Biomaterials 33 (2012) 5584–5592.
- [58] L.L. Tan, H. Li, Y. Zhou, Y. Zhang, X. Feng, B. Wang, Y.W. Yang, Zn<sup>2+</sup>-triggered drug release from biocompatible zirconium MOFs equipped with supramolecular gates, Small 11 (2015) 3807–3813.
- [59] Z. Yuan, P. Liu, Y. Liang, B. Tao, Y. He, Y. Hao, W. Yang, Y. Hu, K. Cai, Investigation of osteogenic responses of Fe-incorporated micro/nano-hierarchical structure on titanium surface, J. Mater. Chem. B 6 (2018) 1359–1372.